J Mater Sci (2020) 55:11086–11094

Advanced Nano Materials

Ni incorporation in $MgFe_2O_4$ for improved CO_2-splitting activity during solar fuel production

Gorakshnath Takalkar[1], Rahul R. Bhosale[1,*], Fares AlMomani[1], Suliman Rashid[1], and R. A. Shakoor[2]

[1] Department of Chemical Engineering, College of Engineering, Qatar University, P.O. Box 2713, Doha, Qatar
[2] Center for Advanced Materials (CAM), Qatar University, P.O. Box 2713, Doha, Qatar

Received: 24 January 2020
Accepted: 5 May 2020
Published online: 25 May 2020

ABSTRACT

Efficacy of the sol–gel derived Ni-doped Mg-ferrites for an enhanced CO_2 splitting activity is investigated. The results allied with the characterization indicate the formation of nominally phase pure Ni-doped Mg-ferrites with a coarser particle morphology. Ni-doped Mg-ferrites are further tested for multiple thermal reduction as well as CO_2 splitting steps by using a thermogravimetric analyzer. The results associated with the thermogravimetric analysis confirmed that most of the Ni-doped Mg-ferrites attained a steady TR aptitude after crossing the 5th or 6th cycle. Likewise, the CS capability of all the Ni-doped Mg-ferrites accomplished consistency after 4th cycle (except for $Ni_{0.11}Mg_{0.88}Fe_{2.01}O_{4.005}$). The $Ni_{0.90}Mg_{0.11}Fe_{2.04}O_{4.070}$ showed the highest amount of O_2 release (117.1 µmol/g cycle) and CO production (210.3 µmol/g cycle) in ten consecutive thermochemical cycles. Besides, $Ni_{0.29}Mg_{0.72}Fe_{1.98}O_{3.980}$ indicated better re-oxidation aptitude (n_{CO}/n_{O_2} ratio = 1.89) when compared with other Ni-doped Mg-ferrites.

Introduction

Production of solar fuels, such as H_2 or syngas, via a metal oxide (MO) based two-step solar thermochemical H_2O/CO_2 cycle (STC) has emerged as one of the promising technologies [1–3]. H_2 can be used directly as a fuel [4], whereas the syngas can be converted into liquid fuels via a catalytic Fischer–Tropsch process [5]. With the help of solar fuel technology, the excessive utilization of fossil fuels and the continuous CO_2 emissions can be reduced. Besides, this technology can store the abundantly available solar energy in the form of liquid fuels such as gasoline, kerosene, and others.

In STCs, the MO plays a vital role in terms of the release and storage of the O_2. The O_2 gets released from the MOs during a thermal reduction (TR) step. On the other hand, the MOs can regain the O_2 during the H_2O/CO_2 (WS/CS) splitting reaction. In previous studies, a variety of MOs has been utilized for the thermochemical conversion of H_2O and CO_2, which mainly includes zinc oxide [6, 7], tin oxide [8, 9], iron oxide [10, 11], CeO_2 [12, 13], doped ceria materials [14, 15], ferrites [16–20], and La-based perovskites

Address correspondence to E-mail: rahul.bhosale@qu.edu.qa; rrbhosle@yahoo.com

https://doi.org/10.1007/s10853-020-04794-1

[21–23]. Among the listed MOs, CeO_2 is considered as a state-of-the-art material for the STCs due to its favorable reaction kinetics and high-temperature stability.

Recently, Takalkar et al. [24, 25] investigated the sol–gel derived Ni-ferrite and Mg-ferrite for the thermochemical splitting of CO_2. The reported results indicate that both Ni-ferrite (64.4 µmol of O_2/g cycle) and Mg-ferrite (58.7 µmol of O_2/g cycle) were capable of releasing higher levels of O_2 than CeO_2 (48.5 µmol of O_2/g cycle) [26] at 1400 °C. The amount of CO produced at 1000 °C by the Ni-ferrite (125.9 µmol of CO/g cycle) was higher and by the Mg-ferrite (79.6 µmol of CO/g cycle) was lower than CeO_2 (95.0 µmol of CO/g cycle). The obtained results show that both Ni-ferrite and Mg-ferrite possess a better TR aptitude than CeO_2. In contrast, work needs to be done to improve the CS ability of the Mg-ferrite.

To utilize the TR capacity of both Ni-ferrite and Mg-ferrite together and to improve the CS ability of the Mg-ferrite, in this study, we have examined ternary Ni-doped Mg-ferrites ($Ni_xMg_{1-x}Fe_2O_{4-\delta}$) in multiple thermochemical cycles. It is believed that the incorporation of Ni in the Mg-ferrite crystal structure (partially replacing Mg^{+2} by Ni^{+2}) will significantly improve the CS aptitude. The redox reactions associated with the two-step Ni-doped Mg-ferrite (NMF) based CS cycle are as follows:

$$Ni_xMg_{1-x}Fe_2O_4 \rightarrow Ni_xMg_{1-x}Fe_2O_{4-\delta} + \delta/2O_2 \quad (1)$$

$$Ni_xMg_{1-x}Fe_2O_{4-\delta} + CO_2 \rightarrow Ni_xMg_{1-x}Fe_2O_4 + CO \quad (2)$$

Ni-doped Mg-ferrites were tested by performing ten thermochemical cycles in which the TR and CS steps were carried out in the temperature range of 1000–1400 °C. Obtained results indicate that most of the Ni-doped Mg-ferrites attained the redox stability after crossing the 4th or 5th thermochemical cycle. This paper reports a detailed analysis of the results obtained during synthesis, characterization, and thermochemical cycles.

Experimental section

Preparation of Ni-doped Mg-ferrites

Ni-doped Mg-ferrites were synthesized by using the sol–gel approach. The stoichiometric amounts of precursors, i.e., nickel nitrate, magnesium nitrate, and iron nitrate (procured from Sigma Aldrich), were first dissolved in ethanol at room temperature. Subsequently, a predetermined quantity of propylene oxide (purchased from Sigma Aldrich) was added into the mixture. The as-prepared solution was kept undisturbed for the formation of the Ni-doped Mg-ferrite gel. The as-synthesized gel was aged and then dried at 120 °C for 2 h. The dried Ni-doped Mg-ferrite was then crushed into a fine powder by using a mortar and pestle. Annealing of the powered Ni-doped Mg-ferrite up to 1000 °C for 4 h was performed by using a muffle furnace.

Characterization of Ni-doped Mg-ferrites

Crystallographic analysis of the Ni-doped Mg-ferrites was carried out by using a Powder X-ray Diffractometer (PXRD) with CuKα radiation, the irradiation time of 5 s, and Bragg angle from 25° to 70° (Panalytical XPert MPD/DY636, λ = 0.15,418 nm, steps = 0.05°). The microstructural morphology and elemental/chemical composition of the Ni-doped Mg-ferrites were scrutinized by using a scanning electron microscope (SEM, Nova Nano 450, FEI) equipped with an energy-dispersive X-ray spectroscopy (EDS).

Cyclic CO_2 splitting test

A CO_2 splitting cyclic study which comprised of multiple TR and CS steps was performed by using a TGA (procured from Setaram SETSYS Evolution, France, Fig. 1). The TGA setup was equipped with two mass flow controllers and a vacuum gauge. The temperature cooling and heating rates were normalized at 25 K/min. The mass variation observed during the TR and CS steps was recorded by using an inbuilt Calisto processing software supplied by the Setaram. During the TGA experiments, approximately 50 mg of the Ni-doped Mg-ferrite powder was loaded on an alumina crucible and placed inside the TGA. Multiple thermochemical cycles were performed by maintaining the operating conditions as follows: a) TR at 1400 °C for 60 min with an Ar flow rate at 100 ml/min and b) CS at 1000 °C for 30 min with an Ar/CO_2 (50:50) mixture flow rate at 100 ml/min. The mass variation recorded by the software was further converted into the amounts of O_2 released and CO produced by using the following equations. Additional details associated with the

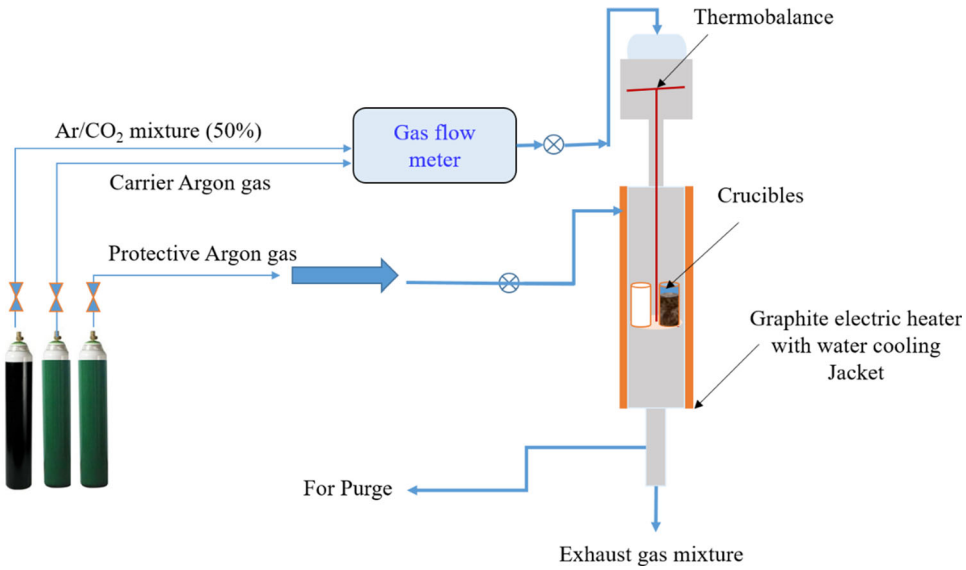

Figure 1 A high-temperature TGA setup (Setaram SETSYS Evolution, France).

other essential parts of the TGA setup and the experimental procedure are listed in our previous contributions [24, 25].

$$n_{O_2} = \frac{\Delta m_{loss}}{(M_{O_2} \times m_{NMF})} \quad (3)$$

$$n_{CO} = \frac{\Delta m_{gain}}{(M_O \times m_{NMF})} \quad (4)$$

where n_{O_2} = moles of O_2 released (μmol/g); n_{CO} = moles of CO produced (μmol/g); Δm_{loss} = amount of loss in the mass (mg); Δm_{gain} = amount of gain in the mass (mg); M_{O_2} = molecular weight of O_2 (g/mol); M_O = molecular weight of O (g/mol); m_{NMF} = mass of the Ni-doped Mg-ferrites (mg)

Results and discussion

The prime objective of this study is to identify the best combination of the Ni-doped Mg-ferrite, which shows better redox performance as compared to CeO_2, Ni-ferrite, and Mg-ferrite. Different combinations of the Ni-doped Mg-ferrites, which includes $Ni_{0.1}Mg_{0.9}Fe_2O_4$ (NMF19), $Ni_{0.3}Mg_{0.7}Fe_2O_4$ (NMF37), $Ni_{0.5}Mg_{0.5}Fe_2O_4$ (NMF55), $Ni_{0.7}Mg_{0.3}Fe_2O_4$ (NMF73), and $Ni_{0.9}Mg_{0.1}Fe_2O_4$ (NMF91), were synthesized by using the sol–gel method. The calcined Ni-doped Mg-ferrites were first analyzed by using PXRD, and the results obtained are reported in Fig. 2a, b. The PXRD peaks associated with each Ni-doped Mg-ferrite showed strong reflections of the cubic spinel structure with the non-existence of any metal or metal oxide impurities such as Ni, Mg, Fe, NiO, MgO, and Fe_3O_4. It was further noticed that the PXRD peaks were shifted toward a lower 2θ angle as the molar concentration of Ni was increased. As the crystal ionic radii of the Ni^{+2} (83 pm) is smaller than the Mg^{+2} (86 pm), the replacement of the Mg^{+2} by Ni^{+2} is the main reason for the shift in the PXRD peaks toward a lower 2θ angel. This result confirmed the substitution of Mg^{+2} by Ni^{+2} and the formation of a desired Ni-doped Mg-ferrite phase composition. An additional check was conducted by analyzing the Ni-doped Mg-ferrite samples by using an EDS apparatus. The obtained results (listed in Table 1) provide further assurance of the formation of nominally phase pure Ni-doped Mg-ferrites.

In addition to the phase and chemical composition, the morphology of Ni-doped Mg-ferrites was scrutinized via SEM analysis. The SEM analysis established that the variation in the Ni^{+2} and Mg^{+2} molar concentrations has an insignificant influence on the morphology. Ni-doped Mg-ferrites showed coarser particle morphology with a diverse particle size in the range of ~ 100 nm (smallest particle) to ~ 1 micron (largest particle). The exemplified SEM images for the $Ni_{0.29}Mg_{0.72}Fe_{1.98}O_{3.980}$ and $Ni_{0.72}Mg_{0.31}Fe_{1.96}O_{3.970}$ are presented in Fig. 3.

After synthesizing and analyzing the physical properties, the redox reactivity of each Ni-doped Mg-ferrite toward the thermochemical splitting of CO_2 was investigated by using a TGA setup. Firstly, the TR and CS ability of each Ni-doped Mg-ferrite was explored by performing a single thermochemical

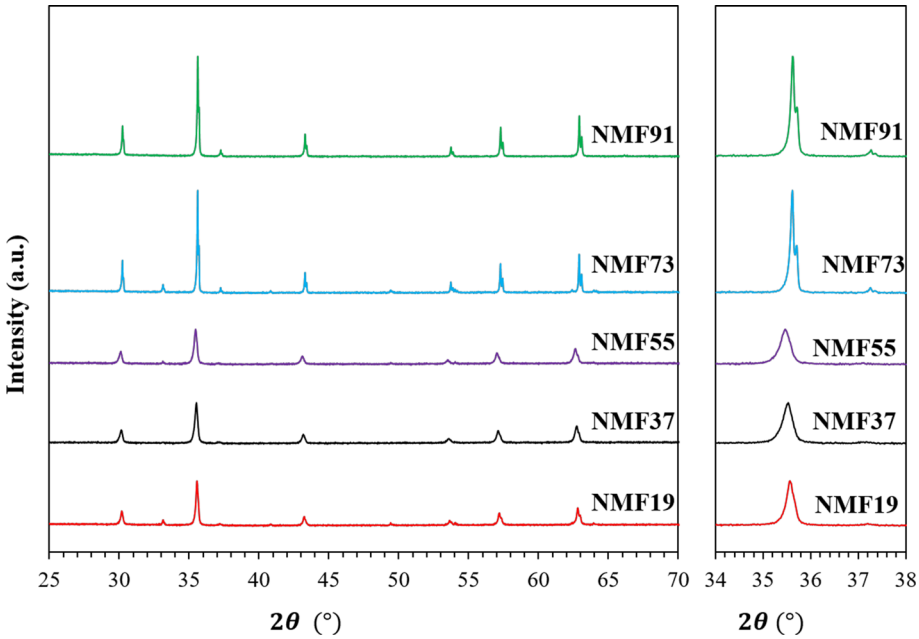

Figure 2 PXRD patterns of Ni-doped Mg-ferrites, **a** $2\theta = 20°$ to 70°, and **b** $2\theta = 34°$ to 38°.

Table 1 Chemical composition of Ni-doped Mg-ferrites

Abbreviation	Ni/Mg/Fe (as-prepared)	Ni/Mg/Fe (from EDS)	Composition
NMF19	0.1/0.9/2.0	0.11/0.88/2.01	$Ni_{0.11}Mg_{0.88}Fe_{2.01}O_{4.005}$
NMF37	0.3/0.7/2.0	0.29/0.72/1.98	$Ni_{0.29}Mg_{0.72}Fe_{1.98}O_{3.980}$
NMF55	0.5/0.5/2.0	0.51/0.50/2.03	$Ni_{0.51}Mg_{0.50}Fe_{2.03}O_{4.055}$
NMF73	0.7/0.3/2.0	0.72/0.31/1.96	$Ni_{0.72}Mg_{0.31}Fe_{1.96}O_{3.970}$
NMF91	0.9/0.1/2.0	0.90/0.11/2.04	$Ni_{0.90}Mg_{0.11}Fe_{2.04}O_{4.070}$

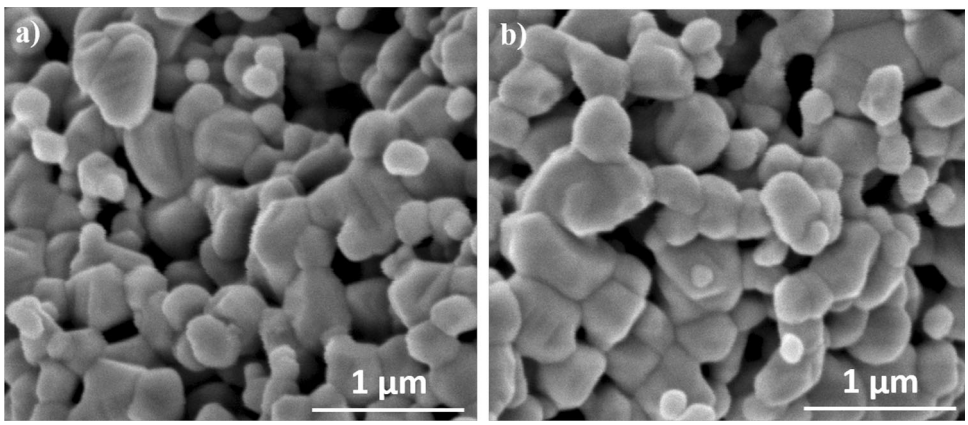

Figure 3 SEM images of **a** $Ni_{0.29}Mg_{0.72}Fe_{1.98}O_{3.980}$, **b** $Ni_{0.72}Mg_{0.31}Fe_{1.96}O_{3.970}$.

cycle, and the TGA profiles obtained are reported in Fig. 4. As expected, Ni-doped Mg-ferrites showed a decrease in the mass during the TR step (due to the release of O_2 and formation of O_2 vacancies) and an increase in the weight during the CS step (via re-oxidation reaction). These mass variations were converted into the n_{O_2} (by using Eq. 3) and n_{CO} (by using Eq. 4) by each Ni-doped Mg-ferrite during 1st cycle (Fig. 5). As per the findings, n_{O_2} by $Ni_{0.90}Mg_{0.11}Fe_{2.04}O_{4.070}$ (327.7 µmol/g) and $Ni_{0.51}Mg_{0.50}Fe_{2.03}O_{4.055}$ (317.9 µmol/g) was considerably higher than the other three Ni-doped Mg-ferrites. Likewise, n_{CO} by $Ni_{0.90}Mg_{0.11}Fe_{2.04}O_{4.070}$ (262.8 µmol/g) was the upmost when compared with other Ni-doped Mg-ferrites. Interesting to note that all the Ni-doped Mg-ferrites showed a higher n_{O_2} as compared to n_{CO}.

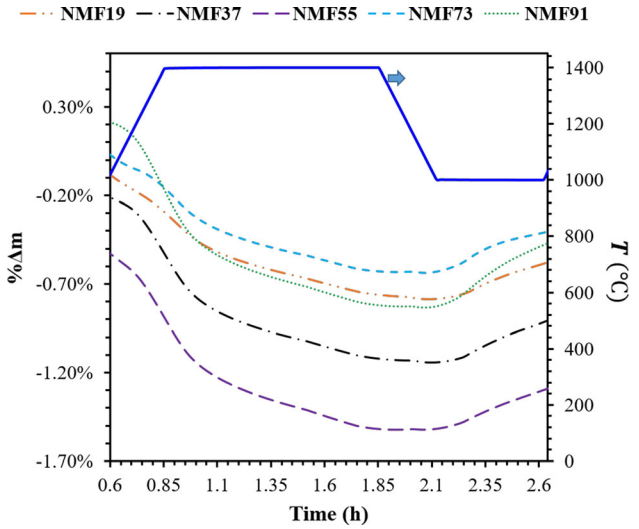

Figure 4 TGA profiles obtained for Ni-doped Mg-ferrites during 1st thermochemical cycle.

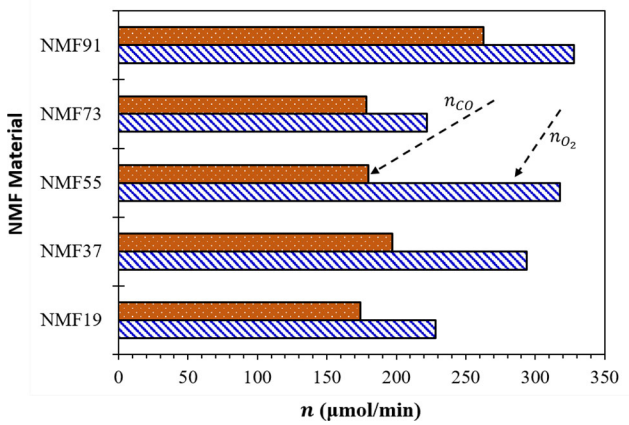

Figure 5 n_{O_2} and n_{CO} by Ni-doped Mg-ferrites during 1st thermochemical cycle.

It is believed that during the high-temperature TR step, the chemicals left over from the synthesis of Ni-doped Mg-ferrites were burned. Due to this burning, an additional drop in the mass was recorded which contributed to the false indication of a higher n_{O_2}. In addition to the role of unburnt chemicals, there is a chance that the re-oxidation capacity of Ni-doped Mg-ferrites was not sizable enough and hence n_{CO} was considerably lower than n_{O_2}. For further exploration, the Ni-doped Mg-ferrites were tested for an additional two thermochemical cycles. TGA profiles obtained for all three cycles are presented in Fig. 6. Besides, a comparison between the three cycles based on n_{O_2} and n_{CO} by Ni-doped Mg-ferrites is presented in Table 2.

Table 2 clearly shows that n_{O_2} by Ni-doped Mg-ferrites was decreased in the 2nd cycle as compared to the 1st cycle. In terms of numbers, n_{O_2} by $Ni_{0.11}Mg_{0.88}Fe_{2.01}O_{4.005}$, $Ni_{0.29}Mg_{0.72}Fe_{1.98}O_{3.980}$, $Ni_{0.51}Mg_{0.50}Fe_{2.03}O_{4.055}$, $Ni_{0.72}Mg_{0.31}Fe_{1.96}O_{3.970}$, and $Ni_{0.90}Mg_{0.11}Fe_{2.04}O_{4.070}$ was reduced by 59.3%, 67.7%, 66.3%, 58.7%, and 59.0%, respectively, in cycle 2 as compared to cycle 1. The above-mentioned results confirmed that the higher levels of n_{O_2} in cycle 1 was due to the release of the volatile matter and burning of the residual chemicals leftover from the synthesis. A further fall in n_{O_2} which was recorded in cycle 3 was considerably lower than the reduction reported in cycle 2. For instance, a decline of about 11.0%, 1.9%, 4.1%, 6.9%, and 4.0% in n_{O_2} by $Ni_{0.11}Mg_{0.88}Fe_{2.01}O_{4.005}$, $Ni_{0.29}Mg_{0.72}Fe_{1.98}O_{3.980}$, $Ni_{0.51}Mg_{0.50}Fe_{2.03}O_{4.055}$, $Ni_{0.72}Mg_{0.31}Fe_{1.96}O_{3.970}$, and $Ni_{0.90}Mg_{0.11}Fe_{2.04}O_{4.070}$ was noticed in cycle 3 when compared with the results obtained in cycle 2.

As shown in Table 2, n_{CO} by Ni-doped Mg-ferrites follows the trend similar to the one observed in the case of n_{O_2}. n_{CO} by $Ni_{0.11}Mg_{0.88}Fe_{2.01}O_{4.005}$, $Ni_{0.29}Mg_{0.72}Fe_{1.98}O_{3.980}$, $Ni_{0.51}Mg_{0.50}Fe_{2.03}O_{4.055}$, $Ni_{0.72}Mg_{0.31}Fe_{1.96}O_{3.970}$, and $Ni_{0.90}Mg_{0.11}Fe_{2.04}O_{4.070}$ was declined by 10.9%, 8.6%, 4.9%, 15.6%, and 11.8%, respectively, in cycle 2 as compared to cycle 1. In cycle 3, however, the percentage decrease in n_{CO} for all Ni-doped Mg-ferrites was extremely lower when compared to cycle 2. The overall results obtained indicate that $Ni_{0.90}Mg_{0.11}Fe_{2.04}O_{4.070}$ possesses better redox reactivity toward the TR and CS reactions than the other Ni-doped Mg-ferrites. The CO production aptitude of all Ni-doped Mg-ferrites was observed to be steady in cycle 2 and cycle 3. However, it was also recorded that the O_2 releasing ability of Ni-doped

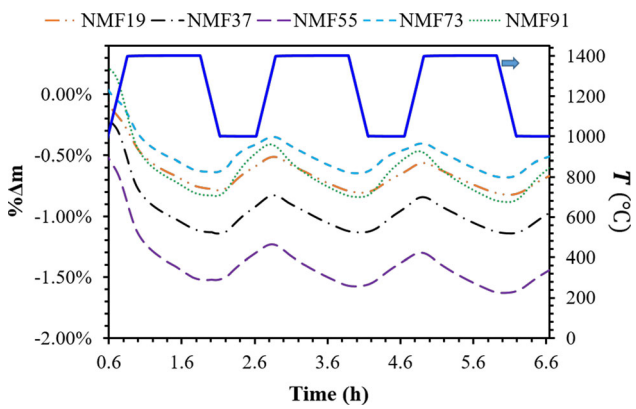

Figure 6 TGA profiles obtained during three consecutive thermochemical cycles.

Table 2 n_{O_2} and n_{CO} by Ni-doped Mg-ferrites during three consecutive thermochemical cycles

NMF Materials	n_{O_2} (μmol/g)			n_{CO} (μmol/g)		
	Cycle 1	Cycle 2	Cycle 3	Cycle 1	Cycle 2	Cycle 3
NMF19	228.3	92.9	82.7	174.3	155.2	156.5
NMF37	294.1	95.0	93.2	197.3	180.3	171.8
NMF55	317.9	107.0	102.6	179.9	171.0	164.7
NMF73	222.3	91.8	85.5	178.6	150.7	139.3
NMF91	327.7	134.4	129.0	262.8	231.9	228.8

Mg-ferrites has not attained stability in the first three cycles.

A set of successive ten thermochemical cycles was carried out to understand the long-term redox reactivity and stability of Ni-doped Mg-ferrites. The experimental conditions were kept unchanged, and the TGA profiles obtained for each Ni-doped Mg-ferrite are reported in Fig. 7. From the results obtained until now it is clear that n_{O_2} by all Ni-doped Mg-ferrites during cycle 1 is not precise. Hence, to avoid publishing any misleading information, the data obtained during the 1st cycle were disregarded, and all the analysis was focused on the remaining nine cycles.

Figure 7 shows the TGA profiles obtained during ten consecutive thermochemical cycles.

The TGA profiles reported in Fig. 7 provide an initial indication that the Ni-doped Mg-ferrites have attained a stable TR and CS ability after crossing cycle 5 or cycle 6. However, it was essential to verify this visual confirmation with the help of numbers. Hence, the mass variations recorded in the TGA profiles were converted into n_{O_2} and n_{CO} with the help of Eqs. (3) and (4).

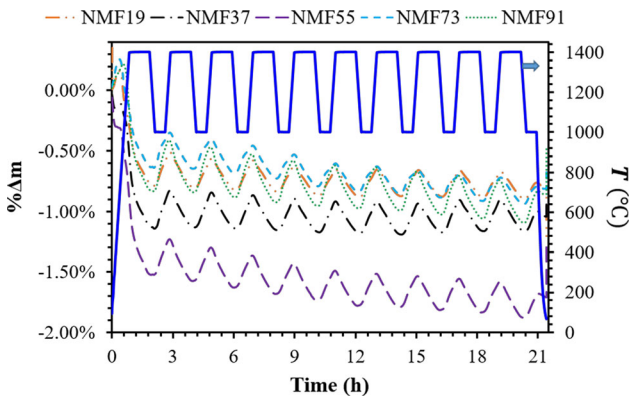

Figure 7 TGA profiles obtained during ten consecutive thermochemical cycles.

n_{O_2} by each Ni-doped Mg-ferrite (from cycle 2 to cycle 10) is presented in Fig. 8. The trends reported supported the visual confirmation provided by Fig. 7 and clearly shows that the Ni-doped Mg-ferrites have attained a steady TR aptitude after surpassing cycle 5 or cycle 6. To be precise, $Ni_{0.11}Mg_{0.88}Fe_{2.01}O_{4.005}$, $Ni_{0.29}Mg_{0.72}Fe_{1.98}O_{3.980}$, $Ni_{0.51}Mg_{0.50}Fe_{2.03}O_{4.055}$, $Ni_{0.72}Mg_{0.31}Fe_{1.96}O_{3.970}$, and $Ni_{0.90}Mg_{0.11}Fe_{2.04}O_{4.070}$ have indicated a stable n_{O_2} once they cross over cycle 6, cycle 5, cycle 6, cycle 4, and cycle 5, respectively. In terms of the average TR ability from cycle 2 to cycle 10, Ni-doped Mg-ferrites can be arranged as follows: $Ni_{0.90}Mg_{0.11}Fe_{2.04}O_{4.070} > Ni_{0.51}Mg_{0.50}Fe_{2.03}O_{4.055} > Ni_{0.29}Mg_{0.72}Fe_{1.98}O_{3.980} > Ni_{0.72}Mg_{0.31}Fe_{1.96}O_{3.970} > Ni_{0.11}Mg_{0.88}Fe_{2.01}O_{4.005}$. The improvement in the TR ability of doped MO depends on the interaction between the metal cations incorporated in the crystal structure. At this moment, we are not in a position to provide any specific reason for the trends reported in Fig. 8 as we have not studied the molecular interaction between the metal cations associated with the Ni-doped Mg-ferrites.

According to Fig. 9, the CS capability of all the Ni-doped Mg-ferrites has attained consistency after crossing cycle 4 except for $Ni_{0.90}Mg_{0.11}Fe_{2.04}O_{4.070}$ for

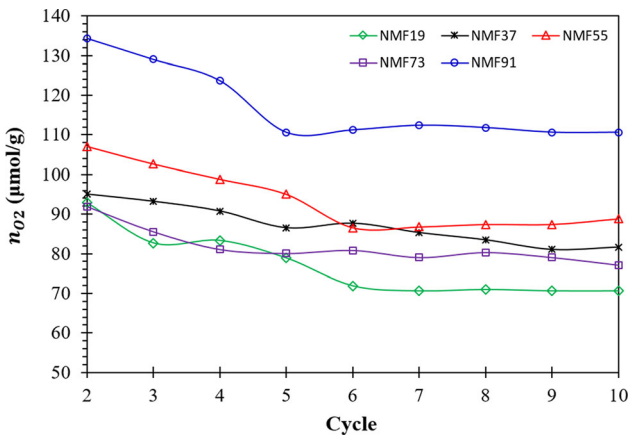

Figure 8 n_{O_2} by Ni-doped Mg-ferrites from cycle 2 to cycle 10.

which a steady n_{CO} was recorded from cycle 5 to cycle 10. In terms of the average n_{CO} from cycle 2 to cycle 10, Ni-doped Mg-ferrites can be ranked as: $Ni_{0.90}Mg_{0.11}Fe_{2.04}O_{4.070}$ > $Ni_{0.29}Mg_{0.72}Fe_{1.98}O_{3.980}$ > $Ni_{0.51}Mg_{0.50}Fe_{2.03}O_{4.055}$ > $Ni_{0.11}Mg_{0.88}Fe_{2.01}O_{4.005}$ > $Ni_{0.72}Mg_{0.31}Fe_{1.96}O_{3.970}$. It is noteworthy that the ranks achieved by Ni-doped Mg-ferrites in the case of CS capability are not identical to the ranks attained in case of the TR aptitude. For instance, $Ni_{0.51}Mg_{0.50}Fe_{2.03}O_{4.055}$ and $Ni_{0.29}Mg_{0.72}Fe_{1.98}O_{3.980}$ have achieved a position of 2nd and 3rd in terms of n_{O_2}. However, based on n_{CO}, $Ni_{0.51}Mg_{0.50}Fe_{2.03}O_{4.055}$ ranked 3rd whereas $Ni_{0.29}Mg_{0.72}Fe_{1.98}O_{3.980}$ has attained the 2nd rank. A similar observation was noticed in the case of $Ni_{0.72}Mg_{0.31}Fe_{1.96}O_{3.970}$ and $Ni_{0.11}Mg_{0.88}Fe_{2.01}O_{4.005}$. In contrast, $Ni_{0.90}Mg_{0.11}Fe_{2.04}O_{4.070}$ was observed to be the best candidate and attained the 1st position among all Ni-doped Mg-ferrites in terms of n_{O_2} and n_{CO}.

As shown in Fig. 10, the average n_{O_2} by Ni-doped Mg-ferrites from cycle 2 to cycle 10 was higher than CeO_2 (48.5 µmol of O_2/g cycle), $NiFe_2O_4$ (64.4 µmol of O_2/g cycle), and $MgFe_2O_4$ (58.7 µmol of O_2/g cycle). In terms of the maximum yield, the TR aptitude of $Ni_{0.90}Mg_{0.11}Fe_{2.04}O_{4.070}$ was recorded to be greater than the CeO_2, $NiFe_2O_4$, and $MgFe_2O_4$ by 68.6 µmol of O_2/g cycle, 52.7 µmol of O_2/g cycle, and 58.4 µmol of O_2/g cycle, respectively. Similar to the TR capacity, the CS ability of Ni-doped Mg-ferrites was superior to CeO_2, $NiFe_2O_4$, and $MgFe_2O_4$ (Fig. 10). The comparison shows that n_{CO} by $Ni_{0.90}Mg_{0.11}Fe_{2.04}O_{4.070}$ was higher than CeO_2, $NiFe_2O_4$, and $MgFe_2O_4$ by a factor of 2.21, 1.67, and 2.64, respectively.

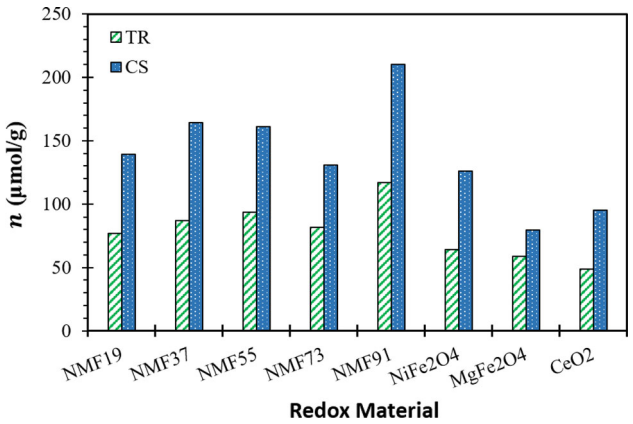

Figure 10 Comparison between Ni-doped Mg-ferrites and CeO_2, $NiFe_2O_4$, and $MgFe_2O_4$ based on the average n_{O_2} and n_{CO}.

Figure 11 shows the variations in the average n_{CO}/n_{O_2} ratio for each Ni-doped Mg-ferrite. As per the data reported, the re-oxidation ability of $Ni_{0.29}Mg_{0.72}Fe_{1.98}O_{3.980}$ was observed to be maximum when compared with other Ni-doped Mg-ferrites. The average n_{CO}/n_{O_2} ratios for the $Ni_{0.11}Mg_{0.88}Fe_{2.01}O_{4.005}$ and $Ni_{0.90}Mg_{0.11}Fe_{2.04}O_{4.070}$ were comparable, whereas $Ni_{0.51}Mg_{0.50}Fe_{2.03}O_{4.055}$ and $Ni_{0.72}Mg_{0.31}Fe_{1.96}O_{3.970}$ indicated the lowest re-oxidation capacity. It was further understood that the average n_{CO}/n_{O_2} ratio of each Ni-doped Mg-ferrite was lower than CeO_2 (average $n_{CO}/n_{O_2} = 1.96$) and the $NiFe_2O_4$ (average $n_{CO}/n_{O_2} = 1.96$). In contrast, the comparison with $MgFe_2O_4$ (average $n_{CO}/n_{O_2} = 1.35$) indicates that the inclusion of Ni^{+2} in the Mg-ferrite crystal structure has improved the average n_{CO}/n_{O_2} ratio of Ni-doped Mg-ferrites.

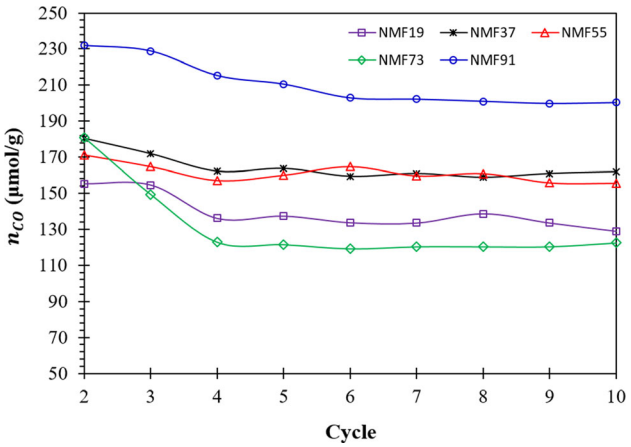

Figure 9 n_{CO} by Ni-doped Mg-ferrites from cycle 2 to cycle 10.

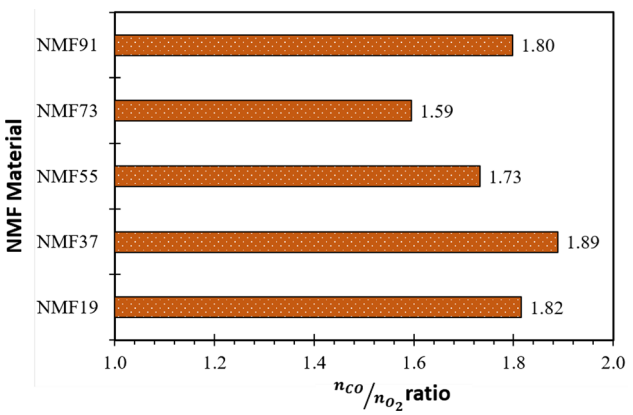

Figure 11 Comparison between Ni-doped Mg-ferrites based on the average n_{CO}/n_{O_2} ratio.

Summary and conclusions

By applying the sol–gel method, Ni-doped Mg-ferrites were synthesized. The PXRD and EDS analysis confirmed the formation of $Ni_{0.11}Mg_{0.88}Fe_{2.01}O_{4.005}$, $Ni_{0.29}Mg_{0.72}Fe_{1.98}O_{3.98}$, $Ni_{0.51}Mg_{0.50}Fe_{2.03}O_{4.055}$, $Ni_{0.72}Mg_{0.31}Fe_{1.96}O_{3.97}$, and $Ni_{0.90}Mg_{0.11}Fe_{2.04}O_{4.07}$. The SEM analysis indicates the formation of coarser particles with sizes in the rage of ~ 100 nm (smallest particle size) to ~ 1 micron (largest particle size). Ni-doped Mg-ferrites were tested in multiple thermochemical cycles by using a TGA (TR at 1400 °C and CS at 1000 °C). Most of the Ni-doped Mg-ferrites indicated stable n_{O_2} and n_{CO} from cycle 5 to cycle 10. In terms of n_{O_2}, Ni-doped Mg-ferrites can be arranged in the following order: $Ni_{0.90}Mg_{0.11}Fe_{2.04}O_{4.07} > Ni_{0.51}Mg_{0.50}Fe_{2.03}O_{4.055} > Ni_{0.29}Mg_{0.72}Fe_{1.98}O_{3.98} > Ni_{0.72}Mg_{0.31}Fe_{1.96}O_{3.97} > Ni_{0.11}Mg_{0.88}Fe_{2.01}O_{4.005}$. Based on their CO production capacity, Ni-doped Mg-ferrites can be ranked as: $Ni_{0.90}Mg_{0.11}Fe_{2.04}O_{4.07} > Ni_{0.29}Mg_{0.72}Fe_{1.98}O_{3.98} > Ni_{0.51}Mg_{0.50}Fe_{2.03}O_{4.055} > Ni_{0.11}Mg_{0.88}Fe_{2.01}O_{4.005} > Ni_{0.72}Mg_{0.31}Fe_{1.96}O_{3.97}$. Ni-doped Mg-ferrites showed higher n_{O_2} and n_{CO} as compared to CeO_2, $NiFe_2O_4$, and $MgFe_2O_4$. In contrast, the average re-oxidation ability of Ni-doped Mg-ferrites was recorded to be lower than CeO_2 and $NiFe_2O_4$, and higher than $MgFe_2O_4$. Our research team is currently exploring the redox ability of Ni-doped Mg-ferrites for more than 100 thermochemical cycles.

Acknowledgements

Open Access funding provided by the Qatar National Library. This publication was made possible by the NPRP Grant (NPRP8-370-2-154) from the Qatar National Research Fund (a member of Qatar Foundation). The statements made herein are solely the responsibility of author(s). The authors also gratefully acknowledge the Center of Advances Materials (CAM) at Qatar University for performing the XRD analysis, the Central Laboratory Unit (CLU) for services related to SEM and EDS.

Compliance with ethical standards

Conflict of Interest The authors declare that they have no conflict of interest.

References

[1] Carrillo RJ, Scheffe JR (2017) Advances and trends in redox materials for solar thermochemical fuel production. Sol Energy 156:3–20

[2] Bhosale RR et al (2019) A decade of ceria based solar thermochemical H_2O/CO_2 splitting cycle. Int J Hydrogen Energy 44:34–60

[3] Lu Y et al (2019) Solar fuels production: two-step thermochemical cycles with cerium-based oxides. Prog Energy Combust Sci 75:100785

[4] Gupta RB (2008) in Hydrogen fuel: production, transport, and storage. Crc Press

[5] Dry ME (2002) The fischer–tropsch process: 1950–2000. Catal Today 71:227–241

[6] Loutzenhiser PG, Steinfeld A (2011) Solar syngas production from CO_2 and H_2O in a two-step thermochemical cycle via Zn/ZnO redox reactions: thermodynamic cycle analysis. Int J Hydrogen Energy 36:12141–12147

[7] Bhosale RR (2018) Thermodynamic efficiency analysis of zinc oxide based solar driven thermochemical H_2O splitting cycle: effect of partial pressure of O_2, thermal reduction and H_2O splitting temperatures. Int J Hydrogen Energy 43:14915–14924

[8] Abanades S, Charvin P, Lemont F, Flamant G (2008) Novel two-step SnO_2/SnO water-splitting cycle for solar thermochemical production of hydrogen. Int J Hydrogen Energy 33:6021–6030

[9] Bhosale RR, Kumar A, Sutar P (2017) Thermodynamic analysis of solar driven SnO_2/SnO based thermochemical water splitting cycle. Energy Convers Manag 135:226–235

[10] Neises M, Roeb M, Schmücker M, Sattler C, Pitz-Paal R (2010) Kinetic investigations of the hydrogen production

step of a thermochemical cycle using mixed iron oxides coated on ceramic substrates. Int J Energy Res 34:651–661

[11] Bhosale RR et al (2015) Solar hydrogen production via thermochemical iron oxide–iron sulfate water splitting cycle. Int J Hydrogen Energy 40:1639–1650

[12] Chueh WC et al (2010) High-flux solar-driven thermochemical dissociation of CO_2 and H_2O using nonstoichiometric ceria. Science 330:1797–1801

[13] Furler P et al (2012) Solar thermochemical CO_2 splitting utilizing a reticulated porous ceria redox system. Energy Fuels 26:7051–7059

[14] Takalkar G et al (2018) Transition metal doped ceria for solar thermochemical fuel production. Sol Energy 172:204–211

[15] Ackermann S, Takacs M, Scheffe J, Steinfeld A (2017) Reticulated porous ceria undergoing thermochemical reduction with high-flux irradiation. Int. J. Heat Mass Transfer 107:439–449

[16] Scheffe JR, Li J, Weimer AW (2010) A spinel ferrite/hercynite water-splitting redox cycle. Int J Hydrogen Energy 35:3333–3340

[17] Gokon N, Takahashi S, Yamamoto H, Kodama T (2008) Thermochemical two-step water-splitting reactor with internally circulating fluidized bed for thermal reduction of ferrite particles. Int J Hydrogen Energy 33:2189–2199

[18] Allen KM, Coker EN, Auyeung N, Klausner JF (2013) Cobalt ferrite in YSZ for use as reactive material in solar thermochemical water and carbon dioxide splitting, part I: material characterization. JOM 65:1670–1681

[19] Allendorf MD, Diver RB, Siegel NP, Miller JE (2008) Two-step water splitting using mixed-metal ferrites: thermodynamic analysis and characterization of synthesized materials. Energy Fuels 22:4115–4124

[20] Bhosale RR, Kumar A, AlMomani F, Alxneit I (2016) Propylene oxide assisted sol–gel synthesis of zinc ferrite nanoparticles for solar fuel production. Ceram Int 42:2431–2438

[21] Scheffe JR, Weibel D, Steinfeld A (2013) Lanthanum–strontium–manganese perovskites as redox materials for solar thermochemical splitting of H_2O and CO_2. Energy Fuels 27:4250–4257

[22] Takacs M et al (2016) Oxygen nonstoichiometry, defect equilibria, and thermodynamic characterization of $LaMnO_3$ perovskites with Ca/Sr A-site and Al B-site doping. Acta Mater 103:700–710

[23] Takalkar G, Bhosale R, AlMomani F (2019) Combustion synthesized $A_{0.5}Sr_{0.5}MnO_{3-\delta}$ perovskites (where, a = La, Nd, Sm, Gd, Tb, Pr, Dy, and Y) as redox materials for thermochemical splitting of CO_2. Appl Surf Sci 489:80–91

[24] Takalkar G, Bhosale RR, AlMomani F (2019) Sol–gel synthesized $NixFe_{3-x}O_4$ for thermochemical conversion of CO_2. Appl Surf Sci 489:693–700

[25] Takalkar G, Bhosale RR (2019) Thermochemical CO_2 splitting using a sol–gel–synthesized Mg-ferrite–based redox system. Int J Energy Res 43(13):6983–6993

[26] Bhosale R, Takalkar G (2018) Nanostructured co-precipitated $Ce_{0.9}Ln_{0.1}O_2$ (Ln = La, Pr, Sm, Nd, Gd, Tb, Dy, or Er) for thermochemical conversion of CO_2. Ceram Int 44:16688–16697